

# Curvature-based energy spectra revealing flow regime changes in Rayleigh-Bénard convection

Michael Mommert<sup>a,\*</sup>, Philipp Bahavar<sup>a</sup>, Robin Barta<sup>a,b</sup>, Christian Bauer<sup>a</sup>,  
Marie-Christine Volk<sup>a</sup>, Claus Wagner<sup>a,b</sup>

<sup>a</sup>*Department Ground Vehicles, Institute of Aerodynamics and Flow Technology, German Aerospace Center, Bunsenstr. 10, 37073, Göttingen, Germany*

<sup>b</sup>*Institute of Thermodynamics and Fluid Mechanics, Technische Universität Ilmenau, 98684, Ilmenau, Germany*

---

## Abstract

We use the local curvature derived from velocity vector fields or particle tracks as a surrogate for structure size to compute curvature-based energy spectra. An application to homogeneous isotropic turbulence shows that these spectra replicate certain features of classical energy spectra such as the slope of the inertial range extending towards the equivalent curvature of the Taylor microscale. As this curvature-based analysis framework is sampling based, it also allows further statistical analyses of the time evolution of the kinetic energies and curvatures considered. The main findings of these analyses are that the slope for the inertial range also appears as a salient point in the probability density distribution of the angle of the vector comprising the two time evolution components. This density distribution further exhibits changing features of its shape depending on the Rayleigh number. This Rayleigh number evolution allows to observe a change in the flow regime between the Rayleigh numbers  $10^7$  and  $10^8$ . Insight into this regime change is gathered by conditionally sampling the salient time evolution behaviours and projecting them back into physical space. Concretely, the regime change is manifested by a change in the spatial distribution for the different time evolution behaviours. Finally, we show that this analysis can be applied to measured Lagrangian particle tracks.

*Keywords:* Rayleigh-Bénard convection, energy spectrum, turbulent energy cascade

---

\*michael.mommert@dlr.de

---

## 1. Introduction

The energy spectrum is one of the classic tools for analysing turbulent flows, as it reveals the energy cascade described by Richardson [1] and allows to observe the extent of scaling laws, such as the one for the inertial range introduced by Kolmogorov [2]. Typically, a Fourier transform is used to compute the relevant relationship of kinetic energy to certain wave numbers. However, the inherently periodic nature of the Fourier transform leads to artefacts when applied to flows in non-periodic domains such as the cubic Rayleigh-Bénard convection cell studied in this paper. For this reason, there are a number of mitigation approaches for spectral solvers that rely on the Fourier transform. Examples include windowing methods [3] or Fourier continuation techniques [4]. In contrast to the use of extensions to the Fourier transform, we pursue an approach for our analysis, where the wavenumber is replaced by the curvature of the velocity vector field as the quantity representing the structure size. Unlike the wavenumber, the curvature is a local property and can therefore be statistically analysed without the implicit requirement of a complete, periodic flow domain. Regarding the calculation of the curvature of the velocity vector field, Theisel [5] gives a definition of the curvature of stationary vector fields. A definition regarding the unsteady nature of flows can be found in the work of Braun et al. [6] for Lagrangian particle tracks, which is transferable to an Eulerian definition of the flow domain. Braun et al. [6] also describe a trend towards higher curvatures with higher Reynolds numbers, a feature expected for a quantity acting as a measure of structure size. This curvature measure has been subject of a number of studies, see e.g. [7, 8, 9]. While Perven et al. [8] investigate the distribution of mean curvatures with a boundary layer, Alards et al. [7] show that the scaling coefficients of the probability density function of curvature in Rayleigh-Bénard convection (RBC) are the same as for homogeneous isotropic turbulence (HIT) as long as the boundary layers are excluded. Hengster et al. [9] confirm this and reveal an anisotropic behaviour of the Cartesian curvature components associated with the anisotropic nature of the RBC flow.

Here, we use the curvature in conjunction with the kinetic energy to study RBC flows. Specifically, we investigate how a change in flow regime manifests itself for the proposed analysis methods in order to shed more light

on the characteristics of the regimes. RBC flows can be classified into flow regimes depending on their main control parameters, the Rayleigh number  $Ra$  and the Prandtl number  $Pr$ . Because of the importance for flows occurring at large scales in nature, a recent focus of investigation has been on the transition from the so-called classical regime to the ultimate regime, which is characterised by strong forcing ( $Ra \gtrsim 10^{11}$ ) and enhanced heat transfer due to fully turbulent boundary layers. A summary of these efforts is given by Lohse and Shishkina [10]. However, since these Rayleigh numbers are difficult to access both numerically and experimentally, we consider a regime transition within the classical regime for the present study. Specifically, we consider a Rayleigh number range  $5 \times 10^5 \leq Ra \leq 10^9$  at a Prandtl number of 0.7. This range was chosen because it covers the transition from boundary layer dominated to bulk dominated thermal dissipation according to the Grossmann-Lohse theory [11, 12] within the classical regime. It also coincides the expected transitions between soft and hard turbulence observed by Heslot et al. [13] and Castaing et al. [14]. Although this accessible range of control parameters has already been extensively studied, the recent study by Castaing et al. [15] shows the potential to refine existing theories of regime transitions.

The methodology for investigating the described parameter range is introduced in section 2.1. First, we use a generic flow pattern (section 2.2) and a HIT dataset provided by the Johns Hopkins Turbulence Databases (JHTDB) (section 2.3) to explore its capabilities. The method is then applied to RBC cases with different  $Ra$  in section 3.1. In addition to discussing the Rayleigh number range  $5 \times 10^5 \leq Ra \leq 10^9$ , we also apply the analysis framework to Lagrangian particle tracking (LPT) data for  $Ra = 2.5 \times 10^9$  and  $Pr = 7$  to investigate its suitability for experimental data in section 3.2.

## 2. Methodology

This section aims to introduce the basics of curvature-based spectra and to explore their characteristics for a segment of the JHTDB HIT dataset ( $Re_\lambda = 433$ ), on which the more extensive analyses are introduced.

### 2.1. Curvature-based energy spectra

For the proposed sampling-based investigation of the relationship between kinetic energy and structure size, both quantities must be calculated for each

sampling point within the domain. In the case of the dimensionless kinetic energy  $E_{\text{kin}}$ , this is a simple dependence on the velocity vector  $\mathbf{u}$ :

$$E_{\text{kin}} = \frac{1}{2} \mathbf{u} \cdot \mathbf{u}. \quad (1)$$

As mentioned in the introduction, the curvature  $\kappa$  [6] is used as a representation of the structure size:

$$\kappa = \|\boldsymbol{\kappa}\| = \left\| \frac{\mathbf{u} \times \left( \frac{\partial \mathbf{u}}{\partial t} + (\mathbf{u} \cdot \nabla) \mathbf{u} \right)}{\|\mathbf{u}\|^3} \right\|. \quad (2)$$

In this definition, the curvature is the magnitude of a curvature vector  $\boldsymbol{\kappa}$  based on the cross product of the velocity of a fluid parcel and its acceleration, i.e. the material time derivative of the velocity. The curvature vector is therefore perpendicular to the plane in which the fluid is curved and its magnitude is equivalent to the reciprocal value to the local radius of curvature. For the purposes of this study, the first step in analysing the relationship between  $E_{\text{kin}}$  and  $\kappa$  is to determine their joint distribution based on the relative incidences. For this, the samples are collected in logarithmically spaced bins of curvature  $B_i^\kappa = [\kappa_{i-1}, \kappa_i[$  and kinetic energy  $B_j^E = [E_{\text{kin } j-1}, E_{\text{kin } j}[$ . The respective relative incidence  $f_{ij}$  is defined as

$$f_{ij} = \frac{\sum_{s=1}^N \mathbb{I}(\kappa_s \in B_i^\kappa, E_{\text{kin } s} \in B_j^E) V_s}{N \sum_{s=1}^N V_s}, \quad (3)$$

where  $s$  is the running index of the samples,  $N$  is the total number of samples,  $V_s$  is the volume each sample represents in the simulation domain used as weight, and  $\mathbb{I}$  is the binary indicator function that returns 1 for samples that belong to the respective bin.

To derive a spectral function  $E_{\text{kin}}(\kappa)$  from this joint distribution, weighted averages of  $E_{\text{kin}}$  are calculated for each  $\kappa$  bin:

$$E_{\text{kin}}(\kappa) = \langle E_{\text{kin}} \rangle_{B_i^\kappa} = \frac{\sum_{s=1}^N E_{\text{kin } s} \mathbb{I}(\kappa_s \in B_i^\kappa) V_s}{\sum_{s=1}^N \mathbb{I}(\kappa_s \in B_i^\kappa) V_s}. \quad (4)$$

## 2.2. Wavenumber-curvature relation

The use of curvature as a measure of flow structure sizes naturally raises the question of how curvature is related to the traditionally used wavenumber of an FFT. For this reason we consider a generic, stationary velocity field



$$u_x(x, y) = \sin(y) \quad (5)$$

$$u_y(x, y) = -\sin(x), \quad (6)$$

that represents a wavenumber of  $k = 1$  in a planar<sup>1</sup>, periodic domain with  $x$  and  $y$  ranging from 0 to  $2\pi$ . A streamline visualisation of the resulting vector field with the respective curvatures coded by colour is displayed in Figure 1. It reveals the characteristic that a single wavenumber is associated with a range of curvatures, including very large values in the centre of the circulation and at the stagnation points, as well as very small values at the interfaces between the synthetic circulations.

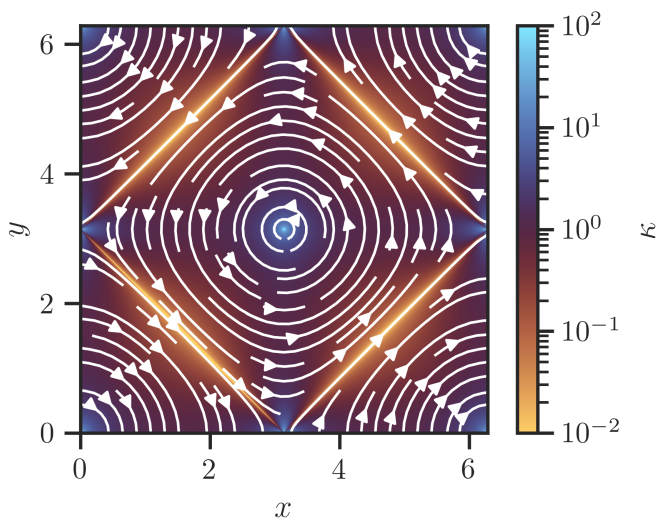


Figure 1: Generic planar flow representing a wavenumber of  $k = 1$ . The respective curvatures  $\kappa$  are coded by color.

Figure 2 shows the corresponding distribution of incidences of  $\kappa$  for spatially homogeneous sampling of this generic velocity vector field. It reveals relatively high constant values for small curvatures up to a curvature of exactly  $\kappa = 1$ , which is the distinct modal value of this distribution. The range from the modal value towards large curvatures shows an exponential

---

<sup>1</sup>We consider a planar domain as sufficient for this investigation since each curvature vector describes a plane in which the rotation is considered.

decay with a slope of  $-3$  which results from the geometry of the circular flow present in the centre of the circulation and near the stagnation points. The derivation of this slope is given in Appendix A. Overall, these results indicate that a wavenumber of  $k = 1$  is associated with a curvature of  $\kappa = 1$  for a domain size of  $2\pi$ . However, this relationship does not imply equality, which means that the distribution of a single wavenumber over a range of curvatures must be taken into account for the subsequent analyses.

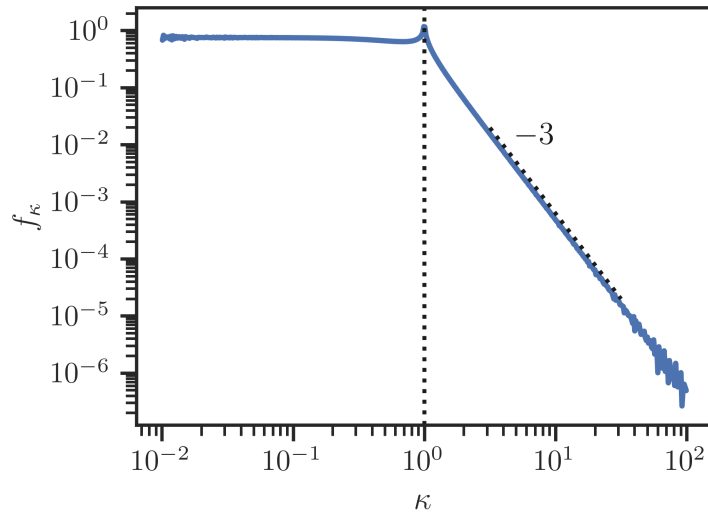


Figure 2: Distribution of incidence of the curvatures for a synthetic planar velocity field with wavenumber  $k=1$  displayed in Figure 1.

### 2.3. Properties of curvature-based spectra for JHTDB HIT

Having established the relationship between wavenumber and curvature, the next step is to explore the properties of the method for a periodic reference case. To do this, we applied the method described above to a case of forced homogeneous isotropic turbulence [16] provided by the JHTDB [17, 18].

The information provided for this flow by the JHTDB includes the classical energy spectrum shown in Figure 3a), as well as the Taylor length scale of  $\lambda = 0.118$  (represented by the dotted lines in Figure 3). In comparison, the curvature-based energy spectrum shown in Figure 3b) was calculated using

the method presented in section 2.1 for a  $32 \times 32 \times 32$  grid segment over 2000 time steps separated by  $\delta t = 0.002$ . All required gradients are calculated by second order accurate finite differences with a central scheme for interior points and a one-sided scheme at the boundaries [19].

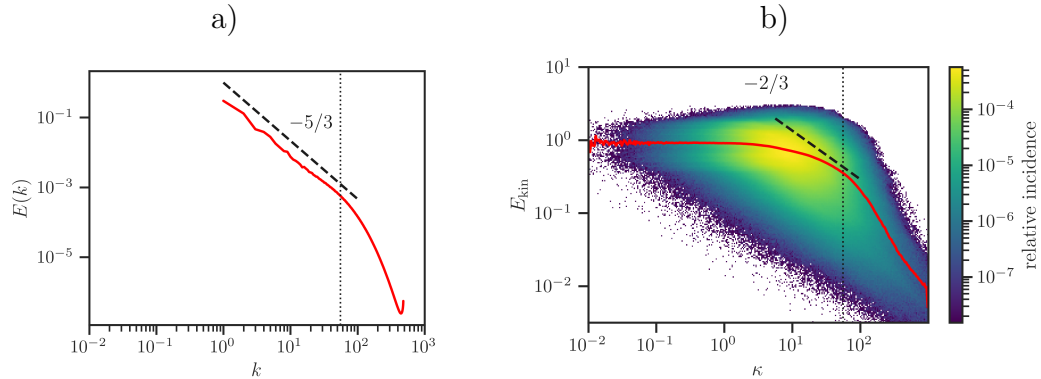


Figure 3: a) Classical energy spectrum for the JHTDB HIT flow provided by [18]. b) Curvature-based energy spectrum based on Equation 4 for a segment of the JHTDB HIT dataset. Dashed lines indicate the respective slopes for the inertial range. The dotted lines mark the abscissa values associated with the Taylor microscale  $\lambda$ .

When comparing the two spectra, it is important to note that the inherent dimensionality of the kinetic energy  $E_{\text{kin}}(\kappa)$  does not include a length dimension stemming from integration, as is the case for  $E(k)$ . Therefore, the expected slope for the inertial range of the curvature spectrum can be derived by

$$E_{\text{kin}} \propto \epsilon^i \kappa^j, \quad (7)$$

$$\frac{\text{length}^2}{\text{time}^2} \propto \left( \frac{\text{length}^2}{\text{time}^3} \right)^i \left( \frac{1}{\text{length}} \right)^j, \quad (8)$$

$$\Rightarrow i = 2/3; j = -2/3, \quad (9)$$

which gives an expected slope of  $-2/3$  for the inertial range of the energy cascade in a curvature-based energy spectrum.

Comparing the two types of energy spectra in Figure 3 shows that the curvature spectrum (b) extends over a wider range of the respective abscissa,

since the theoretical limits of the classical spectrum (a), namely the domain size and the Nyquist wavenumber, do not apply to the curvature. Accordingly, the curvature spectrum exhibits an asymptotic behaviour for  $E_{\text{kin}} \approx 1$  for small curvatures. Together with the relationship between wavenumber and curvature displayed in Figure 2, this results in a rather narrow  $\kappa$  range with the slope of  $-2/3$ . However, the behaviour in conjunction with the Taylor microscale  $\lambda$  appears equal for both types of spectra. In fact, the wavenumbers or curvatures associated with  $\lambda$  (marked by dotted lines) indicate the structure size limit on which viscosity begins to play a significant role. Therefore, both types of spectra show steeper decays than for the inertial range beyond this limit.

This comparison shows that the curvature-based spectrum replicates some of the characteristics of the classical spectrum, although they are not congruent. However, a sampling-based approach also has the advantage that the link to the original data persists and can be used for further analysis. An example of this is the consideration of the time evolution of individual fluid parcels within the  $E_{\text{kin}}-\kappa$  plane, in a visualisation approach similar to the one of Jiménez [20] for different projection variables. To find possible prevalent paths of this time evolution, we again rely on binning statistics. For this, we calculate the time evolution vector

$$\mathbf{U}^* = \left[ \begin{array}{cc} D\kappa/Dt & DE_{\text{kin}}/Dt \\ \ln(10)\kappa & \ln(10)E_{\text{kin}} \end{array} \right]^\top \quad (10)$$

where  $D\phi/Dt$  is the material derivative of an arbitrary scalar  $\phi$ . Note that the normalisation with the respective local values of  $E_{\text{kin}}$  and  $\kappa$  results from considering the vector  $\mathbf{U}^*$  in the double-logarithmic  $E_{\text{kin}}-\kappa$  plane:

$$\phi^* = \log_{10} \phi, \quad (11)$$

$$D\phi^*/Dt = \frac{D\phi/Dt}{\ln(10)\phi}. \quad (12)$$

Similar to Equations 3 and 4, we calculate the resulting vector field  $\mathbf{U}^*(\kappa, E_{\text{kin}})$  by means of bin averages

$$\mathbf{U}^*(\kappa, E_{\text{kin}}) = \langle \mathbf{U}^* \rangle_{B_i^\kappa, B_j^E} = \frac{\sum_{s=1}^N \mathbf{U}_s^* \mathbb{I}(\kappa_s \in B_i^\kappa, E_{\text{kin } s} \in B_j^E) V_s}{\sum_{s=1}^N \mathbb{I}(\kappa_s \in B_i^\kappa, E_{\text{kin } s} \in B_j^E) V_s}. \quad (13)$$

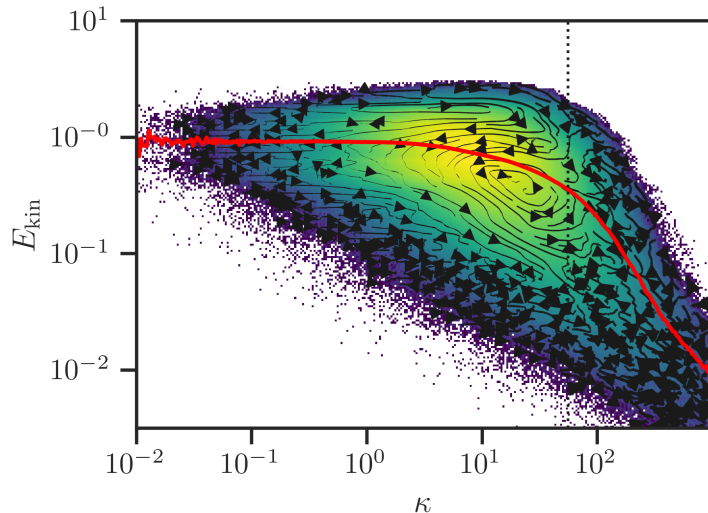


Figure 4: Curvature-based energy spectrum for HIT from Figure 3 extended by a streamline visualization of the mean time evolution vector field  $\langle \mathbf{U}^* \rangle_{B_i^F, B_j^F}$ .

Figure 4 shows a streamline visualisation of the resulting vector field of  $\mathbf{U}^*$  in the  $E_{\text{kin}}-\kappa$  plane. Coherent patterns are particularly evident in regions of high relative incidence. However, due to the limited size of the analysed segment of the dataset, this plot is still state-dependent rather than revealing a completely converged mean process. Nevertheless, the existence of coherent structures of  $\mathbf{U}^*$  raises the question of whether laws such as the  $-2/3$  slope are not only prevalent in a statistical sense, but also for the time evolution. To investigate this, we first define the angular direction  $\theta$  of each vector  $\mathbf{U}^*$  by

$$\theta = \text{atan2}(U_{E_{\text{kin}}}^*, U_{\kappa}^*). \quad (14)$$

As large magnitudes of  $\mathbf{U}^*$  represent large changes within short time spans, a certain effective motion within the  $E_{\text{kin}}-\kappa$  plane is less likely to be sampled for large  $\|\mathbf{U}^*\|$ . To correct this effect, we added  $\|\mathbf{U}^*\|$  to the weighting for the densities  $p_i$  of each angular bin  $B_i^\theta = [\theta_{i-1}, \theta_i[$  with widths  $\Delta_i$ :

$$p_i = \frac{\sum_{s=1}^N \mathbb{I}(\theta_s \in B_i^\theta) V_s \|\mathbf{U}_s^*\|}{\Delta_i \sum_{s=1}^N V_s \|\mathbf{U}_s^*\|}. \quad (15)$$

The resulting polar density distribution is displayed in Figure 5. It reveals a bimodal distribution with two peaks at the angles 0 and  $\pm\pi$ , corresponding to an evolution of the curvature towards larger or smaller values, respectively, without significant changes in the kinetic energy. Thus, these peaks are associated with ideal inertial behaviour, where the curvature changes of the trajectory of a fluid parcel do not result in any acceleration or deceleration along its path. Furthermore, the polar histogram exhibits rotational symmetry, with both peaks being clock-wise skewed. Interestingly, the shoulders that characterise this skew extend to the respective angles associated with the  $-2/3$  slope, which is marked by a dotted line. Beyond these angles, the densities decrease more rapidly.

### 3. Rayleigh-Bénard data

#### 3.1. Rayleigh number variation

Using the curvature spectrum analysis introduced for the case of HIT, we now turn to RBC in a cubic domain to study the evolution of its characteristics in the context of flow regime changes. To do this, we focus on the Rayleigh number dependence for a given Prandtl number of  $Pr = 0.7$ . The data sets considered for this investigation are listed in Table 1. These data sets have been generated by a fourth-order DNS solver that has been validated for a variety of flows. RBC examples include the studies of Shishkina and Wagner [21], Kaczorowski and Wagner [22], Kaczorowski and Xia [23].

As the presented analysis of curvature spectra is based on sampling, we aimed to consider the same number of sampling points, specifically  $N \approx 3.2 \times 10^9$ , for each case. This results in a large variation of the considered time intervals between small and large Rayleigh numbers, which is addressed in Appendix B to show that the discussed statistics are not time interval sensitive and sufficiently converged.

As an overview of these cases, Figure 6 displays exemplary, instantaneous fields of colour-coded temperatures within a vertical central section of the domain. They are complemented by randomly sampled vectors representing

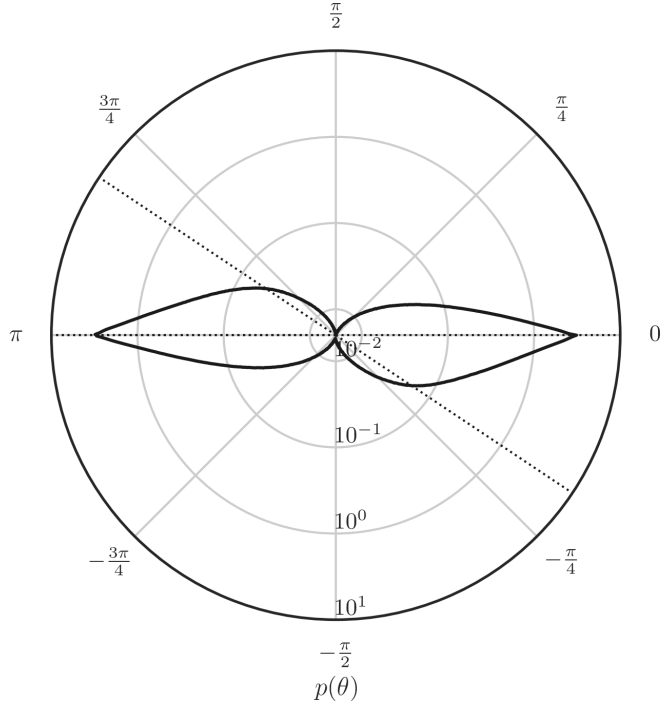


Figure 5: Polar density distribution of the angle  $\theta$  of the time evolution vector  $\mathbf{U}^*$  for the JHTDB HIT flow case. The angle associated with the  $-2/3$  slope is marked by a dotted line.

the in-plane velocity components. Overall, they show the presence of a large-scale circulation (LSC) and the increase in intricacy, i.e. smaller structure sizes, with increasing Rayleigh number.

As a first step in the analysis, the line spectra of each case are calculated according to Equation 4. They are plotted in Figure 7, where the scales associated with the domain size are marked by two dash-dotted lines referring to the curvatures of the spheres circumscribing and inscribing the cubic domain. The comparison between the cases reveals that they all exhibit a similar maximum energy of  $E_{\text{kin}} \approx 0.03$  for curvatures just above those associated with the domain size. For smaller curvatures, they all display a constant behaviour with increasing  $E_{\text{kin}}$  values with increasing Rayleigh number. For curvatures associated with the domain size and higher values, all cases initially exhibit the  $-2/3$  slope of the inertial range before showing the bend towards a steeper slope with the onset of viscous effects. This turn-

Pr	Ra	$N_x \times N_y \times N_z$	$N_t$	$\delta t$
0.7	$5 \times 10^5$	$64 \times 64 \times 64$	12096	0.01
0.7	$10^6$	$96 \times 96 \times 96$	3584	0.01
0.7	$10^7$	$160 \times 160 \times 160$	774	0.01
0.7	$10^8$	$384 \times 384 \times 384$	56	0.01
0.7	$10^9$	$768 \times 768 \times 768$	7	0.01

Table 1: Overview over the investigated RBC cases. The number of available time frames  $N_t$  with a separation of  $\delta t$  is adjusted, so that approximately  $3.2 \times 10^9$  overall samples are considered for each case.

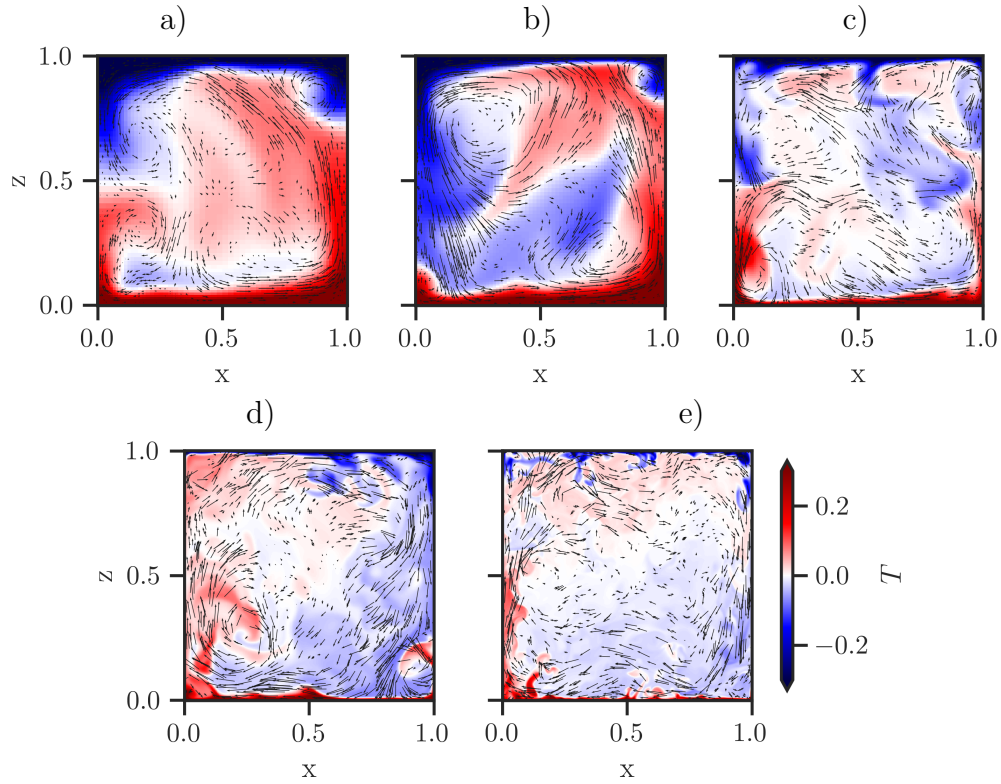


Figure 6: Exemplary fields of the temperature (color-coded) and the in-plane velocity components (vectors) in a central vertical section of the domain. a)  $Ra = 5 \times 10^5$  b)  $Ra = 10^6$  c)  $Ra = 10^7$  d)  $Ra = 10^8$  e)  $Ra = 10^9$ .

ing point is – as expected – shifted towards larger curvatures for the more turbulent, high Ra cases. More specifically, this already occurs at  $\kappa \approx 5$



for the lowest Rayleigh numbers, while it occurs at  $\kappa \approx 100$  for the case of  $Ra = 10^9$ . This feature also leads to higher kinetic energies contained in the larger curvatures for higher Rayleigh numbers. After the inflection point, the  $Ra = 10^8$  and  $Ra = 10^9$  cases further display a consistent slope of  $-6/5$ , while the cases with lower  $Ra$  display slightly steeper declines. Overall, the curvature-based energy spectra display an expected monotonous evolution with respect to the Rayleigh number, underlining the suitability of applying this curvature-based framework to turbulent flows.

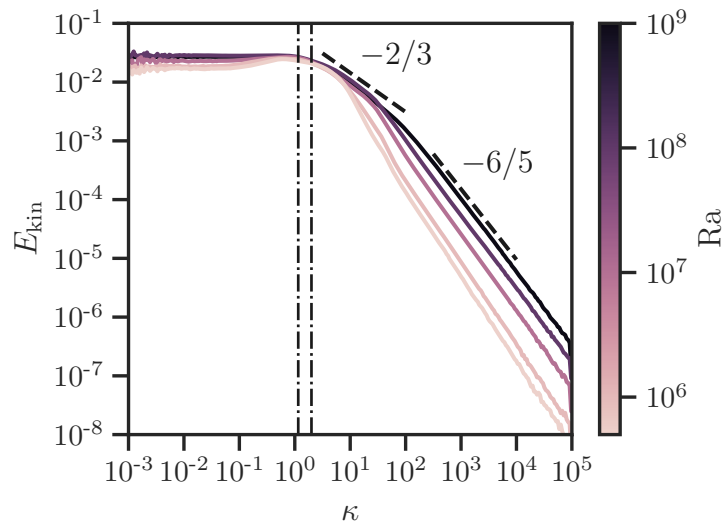


Figure 7: Curvature-based energy spectra for a  $Ra$  variation ranging from  $5 \times 10^5$  to  $10^9$ . Dash-dotted lines indicate the curvature values corresponding to the radii of the circumscribing and inscribing spheres of the cubic domain.

In order to gain a deeper insight into the time evolution of the turbulent structures of the different flow cases, the next step of the analysis is to consider the time evolution vector  $\mathbf{U}^*$  and to derive the respective polar density distributions of its slope angles  $\theta$  with reference to Equations 10 to 15. For the sake of completeness, the streamline visualisations of  $\mathbf{U}^*$  within the  $E_{\text{kin}}-\kappa$  plane are recorded in Appendix C. The respective polar density distributions  $p$  of the angle  $\theta$  of the different Rayleigh numbers are collected in Figure 8. Compared to the energy spectra, these distributions show a more complex behaviour with respect to the dependence on  $Ra$ . Starting from the most turbulent case  $Ra = 10^9$ , two pronounced modal values at 0

and  $\pm\pi$  can be observed, as was the case for HIT. However, in contrast to HIT, the shoulders at the angles associated with the  $-2/3$  slope are significantly more pronounced, which is emphasised by concave sections of  $p(\theta)$ . Moving to  $\text{Ra} = 10^8$ , the density decreases for the peaks on the horizontal, while it increases for the  $-2/3$  slope, even forming secondary peaks. For this  $\text{Ra}$  the section of  $p(\theta)$  between the horizontal and the  $-2/3$  slope are still concave. This changes for  $\text{Ra} = 10^7$ , where the shoulders at the  $-2/3$  slope become rounded and the densities decrease there while they also increase for the horizontal. However, they do not reach the values of  $\text{Ra} = 10^9$ . After that, for  $\text{Ra} = 10^6$  and  $\text{Ra} = 5 \times 10^5$ , the general trend of increasing densities for the  $-2/3$  slope and decreasing densities in the horizontal for decreasing  $\text{Ra}$  is resumed. This goes so far that the peak densities at (for  $\text{Ra} = 10^6$ ) or near (for  $\text{Ra} = 5 \times 10^5$ ) the  $-2/3$  slope have similar levels to the peak in the horizontal.

As discussed for the HIT case, the horizontal peaks represent perfect inertial behaviour of a fluid parcel. Therefore, the  $-2/3$  slope should not be viewed as a representation of the inertial range in the context of the time evolution vector  $\mathbf{U}^*$ . Instead, we associate it with cascading behaviour as it shows a simultaneous increase in curvature and decrease in kinetic energy, and vice versa. Two things are noteworthy in this context. First, that the predicted  $-2/3$  slope is not only statistically prevalent within the energy spectrum, but also plays a significant role in the time evolution experienced by a fluid parcel. Second, that the upward and downward cascading parts of the density distribution are largely rotationally symmetric, suggesting some sort of symmetry of the respective processes within the flow.

In terms of the change in flow regime, the range of Rayleigh numbers studied lies in the region of the transition between soft and hard turbulence described by Castaing et al. [14] and the transition between boundary layer dominated and bulk dominated thermal dissipation described by the Grossmann-Lohse-theory [11, 12]. It is therefore affirming to observe a clear footprint of a transition, in the form of a convex-concave change of the section between the horizontal and the  $-2/3$  slope, associated with the inversion of the evolution of how pronounced the respective densities are.

In order to better understand the effects observed for the density distribution  $p(\theta)$ , we take advantage of another benefit of the persistent link to the original data, namely the possibility of conditional sampling and back-projection. Specifically, we define regions of interest of  $\pm 0.1$  radians around

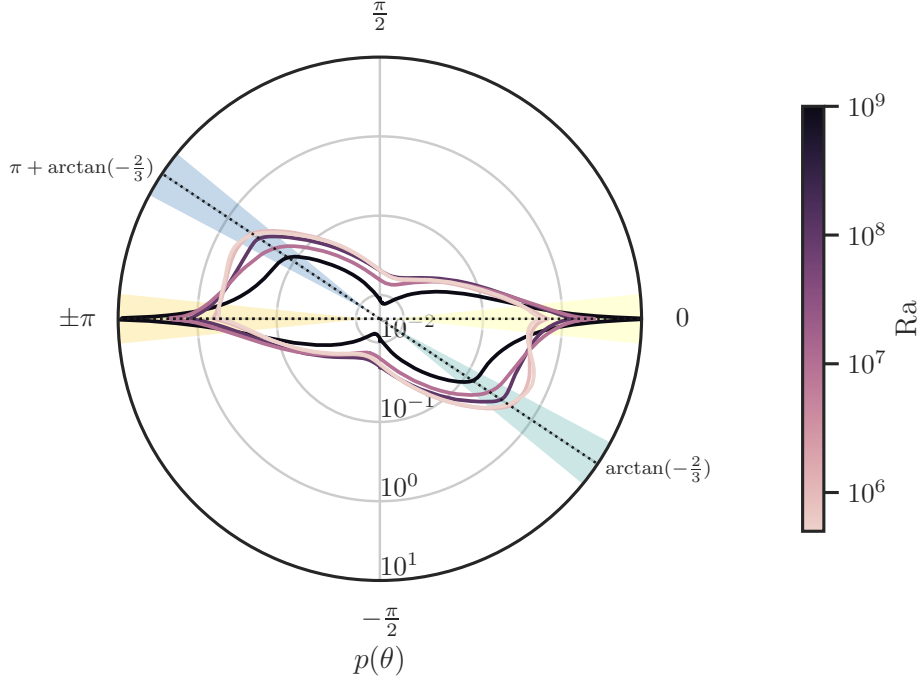


Figure 8: Polar density distributions of the angle  $\theta$  of the time evolution vector  $\mathbf{U}^*$  for a  $Ra$  variation ranging from  $5 \times 10^5$  to  $10^9$ . The angles corresponding to the  $-2/3$  slope are marked by a dotted line. The colored sectors refer to the regions for which, conditional sampling is executed for the back-projections displayed in Figure 9.

the salient angles of  $p(\theta)$ , which are marked in Figure 8 as follows: Yellow indicates the inertial *curving* section opposite to the *straightening* section marked in orange. Similarly, the green section marks *downward cascading* behaviour, while the blue section represents the opposite *upward cascading* behaviour. These segments were then used as conditions to select the samples of the data sets to be back-projected into the physical domain. To give an impression of where these samples are located, their summed densities, i.e. viewing direction-integrated and time-averaged locations, are plotted in Figure 9 for the cases of  $Ra = 10^6$  (left) and  $Ra = 10^9$  (right). To account for the three-dimensional nature of the flow, both horizontal viewing directions,  $y$  (left) and  $x$  (right), are displayed for each case. For orientation, the

first row provides instantaneous pseudo-shadowgraphs, i.e. fields of  $\langle |\nabla^2 T| \rangle_y$  and  $\langle |\nabla^2 T| \rangle_x$ , as they also integrate along the viewing direction and provide information about the diagonal orientation of the LSC.

Examining the back-projections for the  $\text{Ra} = 10^6$  case (left side of Figure 9), it becomes apparent that the purely inertial processes of curving and straightening occur somewhat less frequently than their cascading counterparts. Pure curving appears to be relatively uniformly distributed, but with prominent maxima at the side walls, where plumes begin to curve before impacting the opposing horizontal plates. Minima for curving are visible for regions where the pure straightening has its maxima, namely the impact regions of the top and bottom plates as well as regions at the side walls associated with plume ejection. The minimum regions of the straightening process are mainly occupied by the two cascading processes. For downward cascading, i.e. curving with decreasing kinetic energy, the maxima can be found in the vicinity of the horizontal plates, close to the edges where the plumes detach. However, the minima for this process are located immediately adjacent to the maxima, at the side walls, where the detached plumes straighten. This is also where the maxima for the upward cascade are located, as the fluid is typically accelerated by buoyancy in these regions. In addition to the regions of these maxima, the samples with upward cascading behaviour tend to be found in the bulk region.

On the other side, the  $\text{Ra} = 10^9$  case exhibits density maps with much finer structures, which is due to the short averaging time interval of this case. Nevertheless, the regions where certain processes are concentrated, are already observable. Consistent with the results of the densities of  $p(\theta)$  (see Figure 8), the two purely inertial processes in this case have higher incidences compared to with the lower  $\text{Ra}$ . The maximum regions for the curving and straightening behaviour appear very similar and are located in the vicinity of all the walls, including the horizontal plates. In contrast, the bulk regions are slightly less dense for these processes. The occurrences of the two cascading behaviours are not as similar to each other as the two inertial behaviors. Nevertheless, both display slightly higher densities in the central regions, i.e. the bulk flow.

The key point of this comparison is that the spatial distribution, where the different processes occur, actually changes with the observed change of the flow regime. One aspect of this change is, that the two cascading behaviours switch from having strongly localised maxima close to the walls to a more distributed occurrence in the bulk. This aspect also correlates with the shift

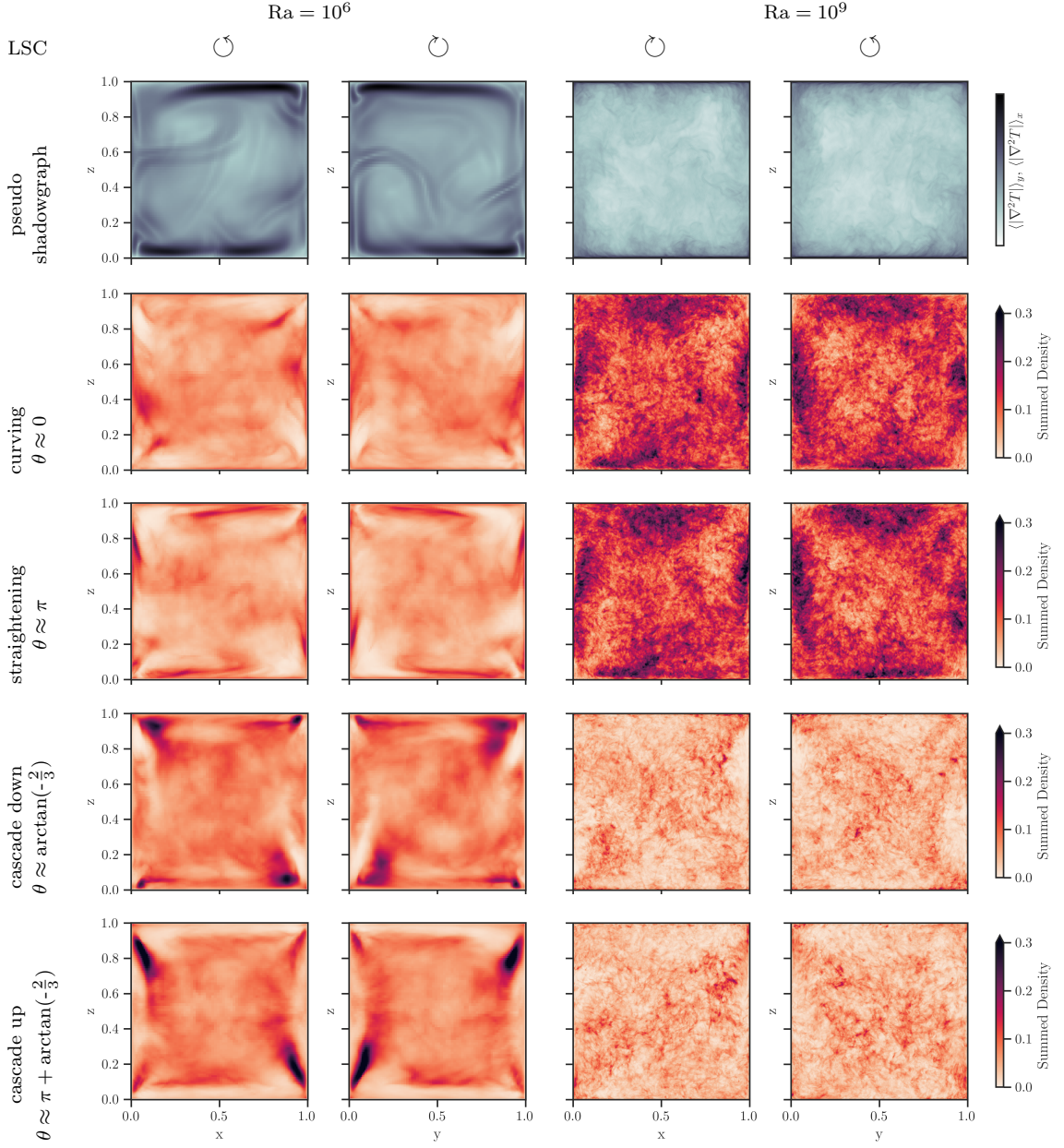


Figure 9: Comparison of the back-projections of the  $\theta$  ranges marked in Figure 8 into physical space for the Rayleigh numbers  $10^6$  (left) and  $10^9$  (right). The first row comprises instantaneous pseudo shadowgraphs ( $\langle |\nabla^2 T| \rangle$ ). For each Ra, two horizontal viewing directions  $y$ -parallel (left) and  $x$ -parallel (right) are presented. Below, the incidence densities for the respective ranges of  $\theta$  are displayed by integrating over the viewing direction and the respective time interval of the data set.

of the dominance of thermal dissipation from the boundary layer to the bulk as described by the Grossmann-Lohse-theory.

### 3.2. PTV data

To demonstrate the feasibility of applying the curvature-based analysis framework to measurement data, we introduce a Lagrangian particle tracking (LPT) dataset with  $Ra = 2.5 \times 10^9$  and  $Pr = 7$ . It is part of the study by Barta and Wagner [24] and was acquired using of the proPTV measurement framework [25]. Figure 10 displays 500 exemplary tracks out of the total of 169428 tracks used for the analysis. These tracks fill an interval of approximately 253 free-fall time units and yield approximately  $2.5 \times 10^7$  samples with a time resolution of  $\delta t \approx 0.042$ . A Savitzky-Golay filter [26] with a polynomial degree of 3 and a window size of 30 time steps has been applied to eliminate measurement noise.

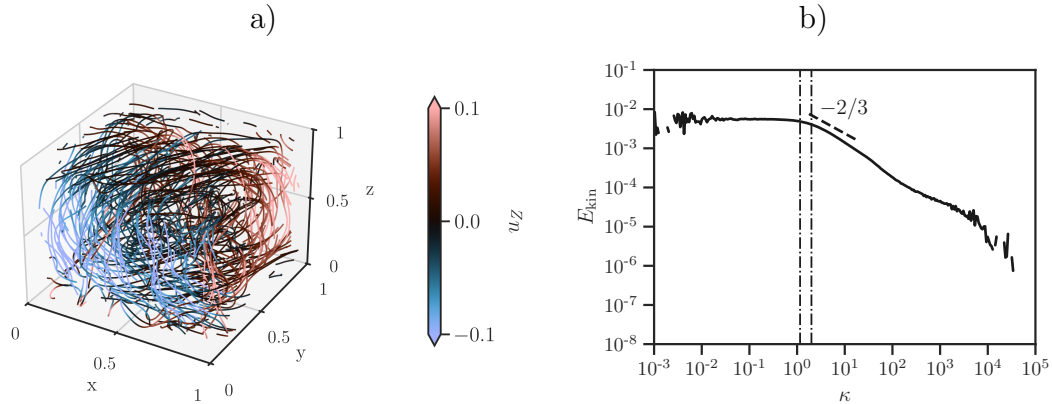


Figure 10: a) Visualization of 500 exemplary particle tracks from the LPT data set. b) Curvature-based energy spectrum of the LPT data set at  $Ra = 2.5 \times 10^9$  and  $Pr = 7$ .

The first step of the analysis is again the calculation of the spectrum  $E_{kin}(\kappa)$  according to Equation 4, which is displayed in Figure 10b). For this, we assume that the tracer particles are uniformly distributed, meaning that the volume weighting was not applied for this case. As for the DNS cases with a lower  $Pr$ , the spectrum shows a constant behaviour in the range of the smallest curvatures up to the curvatures associated with the domain size. From there on, a decrease in the kinetic energy with the  $-2/3$  slope is

observed, which becomes steeper in the region  $10 \lesssim \kappa \lesssim 30$ . At  $\kappa \approx 100$ , the spectrum bends towards less steep slopes again. As there is no viable physical explanation for this, we attribute this behaviour to the inertia of the tracer particles, which also prevents measurements for very high curvatures ( $\kappa \gtrsim 10^4$ ).

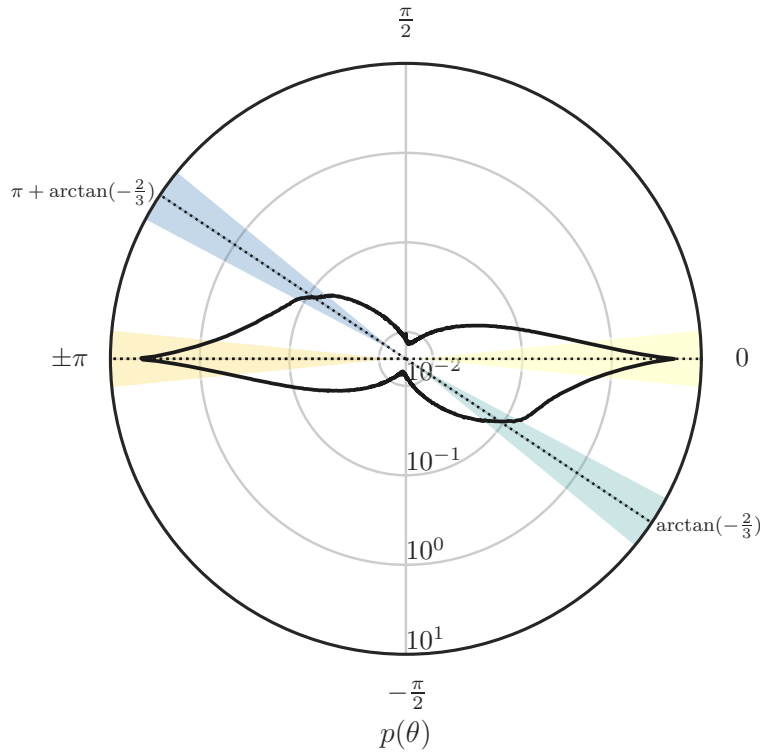


Figure 11: Polar density distribution of the angle  $\theta$  of the time evolution vector  $\mathbf{U}^*$  for the LPT data set at  $\text{Ra} = 2.5 \times 10^9$  and  $\text{Pr} = 7$ .

The next key point of the curvature-based analysis framework is the density distribution  $p(\theta)$  for the time evolution vector  $\mathbf{U}^*$  displayed in Figure 11. As with the curvature spectrum, this polar density distribution plot of the LPT dataset displays features also seen for the DNS dataset of similar Rayleigh number and lower Prandtl number. Specifically, the dominant modal values at angles 0 and  $\pm\pi$  with a concave segment extending up to the angles for the  $-2/3$  slope, where they form a pronounced shoulder, are replicated. Also taking into account possible time resolution effects discussed in

Appendix B, the only qualitative deviation from the DNS results is that the locations of the shoulders do not exactly match the angles of the  $-2/3$  slope. As these locations are slightly shifted towards the horizontal, which represents purely inertial behavior, we also attribute this to the inertial effects of the tracer particles.

#### 4. Conclusion and Outlook

To avoid the spurious effects of an FFT in bounded domains, we introduced an analysis framework based on curvature as a measure of the flow structure size. Its application to homogeneous isotropic turbulence showed that curvature-based energy spectra are able to cover the main characteristics of the flow, such as the slope for the inertial range or the onset of viscous effects, while not being completely congruent with the results provided by classical energy spectra.

We further showed that the persistent link to the raw data is an advantage of this method, which can be exploited to learn about the temporal evolution fluid parcels experience as well as – by means of back-projection – the locations where certain behaviours predominantly occur.

These two features proved to be insightful for the application of the framework to a variety of cases of cubic Rayleigh-Bénard convection, with a Prandtl number of 0.7 and Rayleigh numbers ranging from  $5 \times 10^5$  to  $10^9$ . Within this range, the transition from soft to hard turbulence is expected, as well as a switch from boundary layer-dominated to bulk-dominated thermal dissipation, as described by the Grossmann-Lohse-theory. Using the presented framework, we were able to show the following characteristics of this transition: The curvature-based energy spectra reflect the expected effect of a greater extension of the inertial range for larger Rayleigh numbers and thus overall higher kinetic energies at higher curvatures. For the polar distribution of the time evolution vectors, the transition was more pronounced. While the general trend towards higher Rayleigh numbers pointed towards an increase in the inertial behaviour and a corresponding decrease in the cascading behaviour, this trend was occasionally reversed between  $Ra \approx 10^7$  and  $Ra \approx 10^8$ , together with a significant change in the shape of the distribution.

Subsequently, conditional sampling and back-projection of the various behaviours into the physical domain indeed showed that the cascading behaviour shifts to a less localised and more bulk-centered occurrence during the transition.



Finally, we showed that it is possible to apply this framework to Lagrangian particle tracking data sets, which yielded rational results. This makes this method also appealing for the study of large-scale natural flows, which often have unclear boundaries and are difficult to fully resolve in numerical simulations. Therefore, the observed deficiencies, caused by inertial effects of the tracer particles, need to be overcome to cover a wider range of curvatures. One possible solution would be to combine Lagrangian particle tracking with emerging data assimilation methods using physics-informed neural networks. For these, Toscano et al. [27] and Mommert et al. [28] showed successful applications to thermal convective flows and Zhou and Grauer [29] showed the possibility of extracting the inertial effects of tracer particles.

### **Acknowledgment**

The authors gratefully acknowledge the scientific support and HPC resources provided by the German Aerospace Center (DLR). The HPC system CARO is partially funded by "Ministry of Science and Culture of Lower Saxony" and "Federal Ministry for Economic Affairs and Climate Action".

The authors thank Theo Käufer and Christian Cierpka for the fruitful discussion on the role of the types of curvature definition and the applied time derivative.

### **Declaration of generative AI and AI-assisted technologies in the writing process**

During the preparation of this work the author(s) used DeepL in order to conduct language editing. After using this tool/service, the author(s) reviewed and edited the content as needed and take(s) full responsibility for the content of the publication.

### **Appendix A. Probability density of curvatures for an idealized circulation**

We consider a synthetic, stationary, circular flow centred around an origin, with stream lines effectively forming a set of concentric circles. The radius of curvature of any one circle  $r_i$  is equal to its distance from the origin  $R$ .

Consequently, when sampling the curvatures at points uniformly and at random, the probability of the sample corresponding to a curvature radius

between  $r$  and  $r + dr$  is proportional to the area of the circular ring bounded by circles with radii  $r$  and  $r + dr$ , respectively:

$$P(r, r + dr) \propto \pi(r + dr)^2 - \pi r^2 = 2\pi r dr + \mathcal{O}(dr^2). \quad (\text{A.1})$$

Given the definition of the curvature  $\kappa = 1/r$ ,

$$\frac{dr}{d\kappa} = -\frac{1}{\kappa^2} \Rightarrow dr = -\kappa^{-2} d\kappa. \quad (\text{A.2})$$

Substituting  $r$  and  $dr$  in (A.1) yields the probability density function for the curvature

$$f(\kappa) \propto 2\pi\kappa^{-3}. \quad (\text{A.3})$$

This shows that the exponential decay of the relative incidences towards high curvatures for the synthetic flow representing a wave-number of 1 shown in Figure 1 is a purely geometric one.

## Appendix B. Considerations on temporal convergence

The varying number of time frames  $N_t$  considered naturally raises questions about the convergence of the analyses presented.

The first question concerns whether short time intervals  $N_t \times \delta t$  affect the shape of the polar density distributions  $p(\theta)$  of the angle of the time evolution vector  $\mathbf{U}^*$ . To address this Figure B.12 plots  $p(\theta)$  for a varying number of frames considered  $N_t$ . It shows that even for the smallest number of frames number investigated,  $N_t = 7$ , the deviations from the distribution for  $N_t = 3584$  (black) are minimal and lower  $N_t$  are mainly characterised by more pronounced noise. Therefore, the shape of  $p(\theta)$  appears to be independent of the time interval considered.

The influence of reducing of the frame number on  $p(\theta)$  for the high Rayleigh number case of  $\text{Ra} = 10^9$  is shown in Figure B.13. Here, we investigate the behavior towards the absolute lower end of  $N_t$  with respect to the finite difference differentiation scheme used. Hence, the differences of  $p(\theta)$  for varying  $N_t$  become more apparent: The plot reveals a stronger concentration of  $p(\theta)$  towards the modal values at the angles 0 and  $\pm\pi$  for very small  $N_t$ . We attribute this to the different treatment of the borders of the time interval by the differentiation scheme. This strongly affects  $N_t = 3$

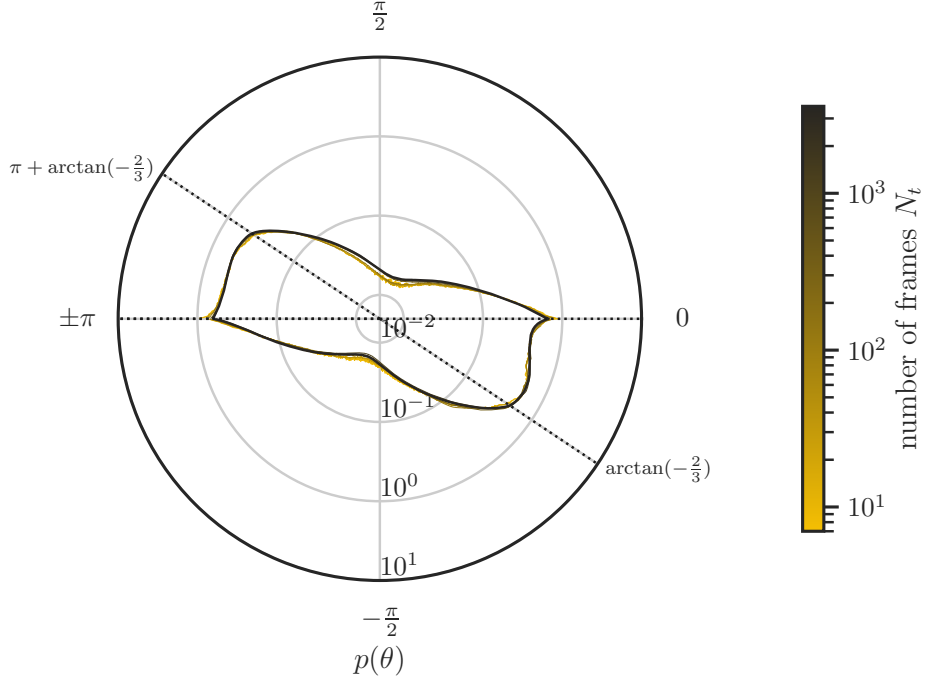


Figure B.12: Polar density distribution of the angle  $\theta$  of the time evolution vector  $\mathbf{U}^*$  for  $\text{Ra} = 10^6$  and varying numbers of frames  $N_t \in \{3584; 1133; 358; 113; 36; 11; 7\}$  considered.

and larger  $N_t$  to a diminishing degree. As the lines of  $N_t = 6$  and  $N_t = 7$  are hardly differentiable, we consider  $N_t = 7$  to be sufficient.

To investigate the influence of the time resolution  $\delta t$  of the provided frames, we regard the case of  $\text{Ra} = 10^8$ , since doubling the frame separation would halve the number of frames drawn from the dataset, which already showed a separate effect in the previous investigation. The corresponding variation in  $\delta t$  is shown in B.14. It reveals the effect that a low time resolution results in more pronounced model values at the angles of 0 and  $\pm\pi$  and less pronounced shoulders or secondary peaks at the angles of the  $-2/3$  slope. However, since  $\delta t = 0.02$  and  $\delta t = 0.01$  are almost congruent, we do not expect significant changes in the shape of  $p(\theta)$  for higher time resolutions.

For the sake of completeness, Figure B.15 displays the curvature-based

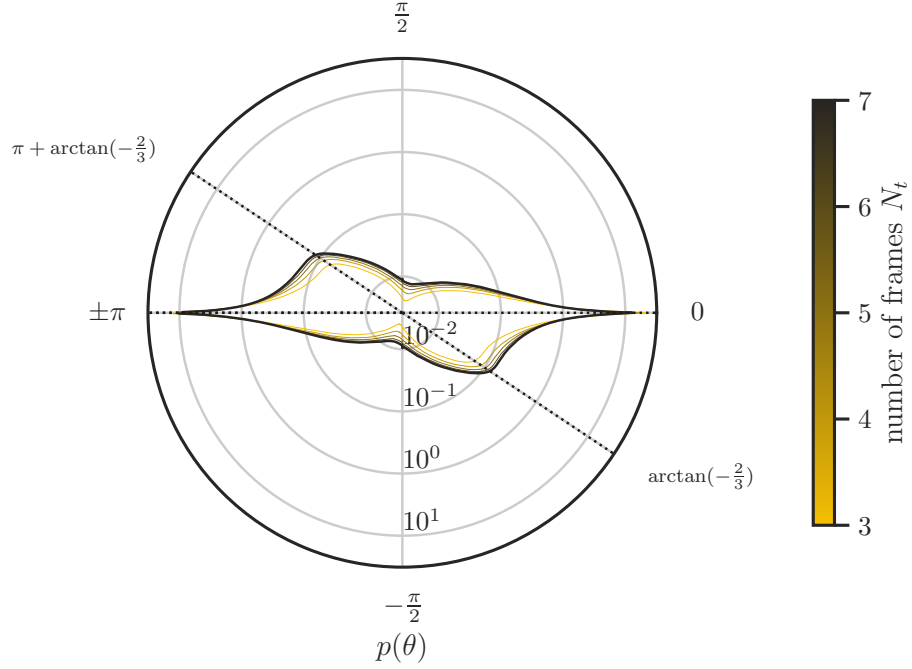


Figure B.13: Polar density distribution of the angle  $\theta$  of the time evolution vector  $\mathbf{U}^*$  for  $\text{Ra} = 10^9$  and varying numbers of frames  $N_t \in \{7; 6; 5; 4; 3\}$  considered.

energy spectra for the sensitivity studies discussed. As these do not rely on the additional time derivative introduced by  $\mathbf{U}^*$ , they are even more robust. Therefore, the only significant deviations visible in these plots are those due to the noise of the inadequate statistics at very low sample counts.

### Appendix C. Streamline visualizations of $\mathbf{U}^*$

Due to the pursued equal number of samples, the widely varying time intervals (see  $N_t$  in Table 1) prohibit a comparison of the prevailing structures of  $\mathbf{U}^*$  within the  $E_{\text{kin}}-\kappa$  plane. Nevertheless, they are displayed in Figure C.16 for the sake of completeness. The existence of the displayed coherent structures implies a statistical dependence between the energy and

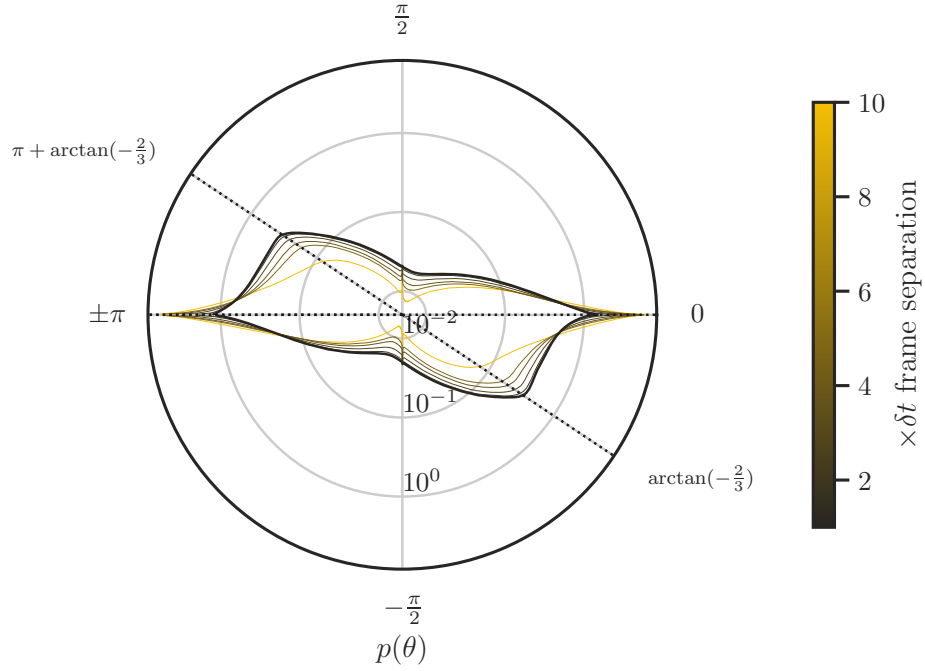


Figure B.14: Polar density distribution of the angle  $\theta$  of the time evolution vector  $\mathbf{U}^*$  for  $\text{Ra} = 10^8$  and varying frame separations  $\delta t \in \{0.01; 0.02; 0.03; 0.04; 0.05; 0.1\}$  considered.

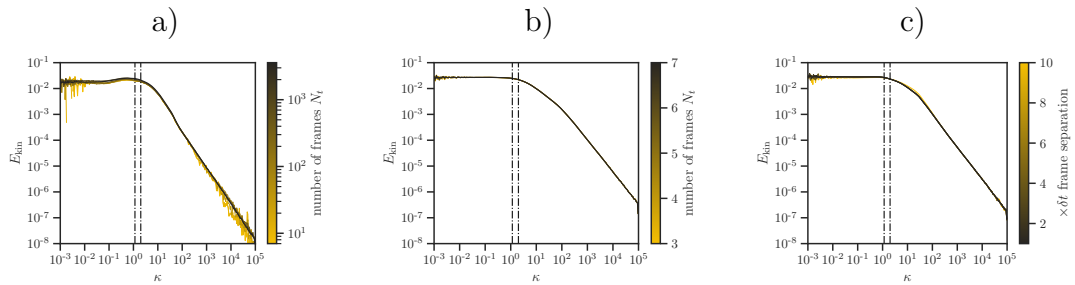


Figure B.15: Curvature-based energy spectra for the sensitivity studies discussed above: a)  $N_t$  variation for  $\text{Ra} = 10^6$  b)  $N_t$  variation for  $\text{Ra} = 10^9$  c)  $\delta t$  variation for  $\text{Ra} = 10^8$ .

curvature evolution of a fluid parcel and its current. In this respect, the circulations close to the maximum of the relative incidence for all cases except  $Ra = 10^9$  are noteworthy. However, their interpretation in terms of the Rayleigh number requires further studies with equal time intervals for each case.

## References

- [1] L. F. Richardson, *Weather Prediction by Numerical Process*, Cambridge University Press, 1922. doi:10.1017/cbo9780511618291.
- [2] A. N. Kolmogorov, The local structure of turbulence in incompressible viscous fluid for very large reynolds numbers, *Proceedings of the Royal Society of London. Series A: Mathematical and Physical Sciences* 434 (1991) 9–13. doi:10.1098/rspa.1991.0075.
- [3] P. Schlatter, N. Adams, L. Kleiser, A windowing method for periodic inflow/outflow boundary treatment of non-periodic flows, *Journal of Computational Physics* 206 (2005) 505–535. doi:10.1016/j.jcp.2004.12.015.
- [4] M. Fontana, O. P. Bruno, P. D. Mininni, P. Dmitruk, Fourier continuation method for incompressible fluids with boundaries, *Computer Physics Communications* 256 (2020) 107482. doi:10.1016/j.cpc.2020.107482.
- [5] H. Theisel, *Vector Field Curvature and Applications*, Ph.D. thesis, Universität Rostock, 1996.
- [6] W. Braun, F. De Lillo, B. Eckhardt, Geometry of particle paths in turbulent flows, *Journal of Turbulence* 7 (2006) N62. doi:10.1080/14685240600860923.
- [7] K. M. J. Alards, H. Rajaei, L. Del Castello, R. P. J. Kunnen, F. Toschi, H. J. H. Clercx, Geometry of tracer trajectories in rotating turbulent flows, *Physical Review Fluids* 2 (2017) 044601. doi:10.1103/physrevfluids.2.044601.
- [8] R. Perven, J. Philip, J. Klewicki, Statistical properties of streamline geometry in turbulent wall-flows, *Physical Review Fluids* 6 (2021) 034609. doi:10.1103/physrevfluids.6.034609.

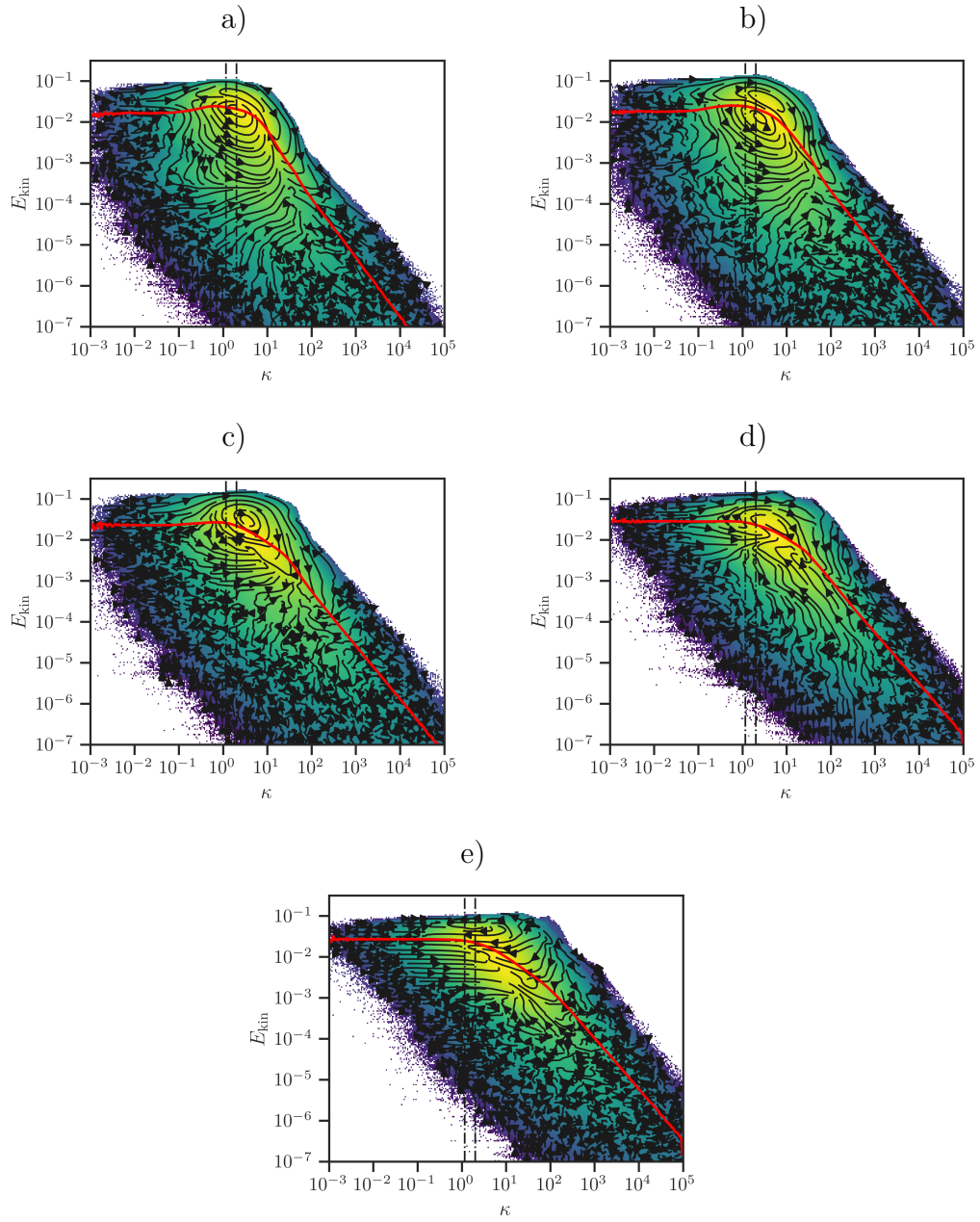


Figure C.16: Streamline visualization for the time evolution vector  $\mathbf{U}^*$  for the various Ra number. The colored background referre to the relative incidence, see Figure 4. a)  $Ra = 5 \times 10^5$  b)  $Ra = 10^6$  c)  $Ra = 10^7$  d)  $Ra = 10^8$  e)  $Ra = 10^9$ .

- [9] Y. Hengster, M. Lellep, J. Weigel, M. Bross, J. Bosbach, D. Schanz, A. Schröder, F. Huhn, M. Novara, D. Garaboa Paz, C. J. Kähler, M. Linkmann, Effects of anisotropy on the geometry of tracer particle trajectories in turbulent flows, *European Journal of Mechanics - B/Fluids* 103 (2024) 284–298. doi:10.1016/j.euromechflu.2023.10.008.
- [10] D. Lohse, O. Shishkina, Ultimate rayleigh-bénard turbulence, *Reviews of Modern Physics* 96 (2024) 035001. doi:10.1103/revmodphys.96.035001.
- [11] S. Grossmann, D. Lohse, Scaling in thermal convection: a unifying theory, *Journal of Fluid Mechanics* 407 (2000) 27–56. doi:10.1017/s0022112099007545.
- [12] R. J. A. M. Stevens, E. P. van der Poel, S. Grossmann, D. Lohse, The unifying theory of scaling in thermal convection: the updated prefactors, *Journal of Fluid Mechanics* 730 (2013) 295–308. doi:10.1017/jfm.2013.298.
- [13] F. Heslot, B. Castaing, A. Libchaber, Transitions to turbulence in helium gas, *Physical Review A* 36 (1987) 5870–5873. doi:10.1103/physreva.36.5870.
- [14] B. Castaing, G. Gunaratne, F. Heslot, L. Kadanoff, A. Libchaber, S. Thomae, X.-Z. Wu, S. Zaleski, G. Zanetti, Scaling of hard thermal turbulence in rayleigh-bénard convection, *Journal of Fluid Mechanics* 204 (1989) 1–30. doi:10.1017/s0022112089001643.
- [15] B. Castaing, F. Chillà, J. Salort, Y. Fraigneau, A. Sergent, The inertial regimes in Rayleigh-Bénard convection. Les régimes inertiels de la convection de Rayleigh-Bénard, 2024. URL: <https://hal.science/hal-04725156>, working paper or preprint.
- [16] W. Minping, S. Chen, G. Eyink, C. Meneveau, P. Johnson, E. Perlman, R. Burns, Y. Li, A. Szalay, S. Hamilton, Forced isotropic turbulence data set (extended), 2012. doi:10.7281/T1KK98XB.
- [17] E. Perlman, R. Burns, Y. Li, C. Meneveau, Data exploration of turbulence simulations using a database cluster, in: *Proceedings of the*



- 2007 ACM/IEEE conference on Supercomputing, SC '07, ACM, 2007, pp. 1–11. doi:10.1145/1362622.1362654.
- [18] Y. Li, E. Perlman, M. Wan, Y. Yang, C. Meneveau, R. Burns, S. Chen, A. Szalay, G. Eyink, A public turbulence database cluster and applications to study lagrangian evolution of velocity increments in turbulence, *Journal of Turbulence* 9 (2008) N31. doi:10.1080/14685240802376389.
- [19] B. Fornberg, Generation of finite difference formulas on arbitrarily spaced grids, *Mathematics of Computation* 51 (1988) 699–706. doi:10.1090/s0025-5718-1988-0935077-0.
- [20] J. Jiménez, Fake turbulence, *Journal of Fluid Mechanics* 990 (2024). doi:10.1017/jfm.2024.516.
- [21] O. Shishkina, C. Wagner, A fourth order finite volume scheme for turbulent flow simulations in cylindrical domains, *Computers & Fluids* 36 (2007) 484–497. doi:10.1016/j.compfluid.2006.02.001.
- [22] M. Kaczorowski, C. Wagner, Study on the Resolution Requirements for DNS in Turbulent Rayleigh-Bénard Convection, in: M. Deville, T. Lê, P. Sagaut (Eds.), *Turbulence and Interactions. Notes on Numerical Fluid Mechanics and Multidisciplinary Design*, volume 110, Springer Berlin Heidelberg, 2010, pp. 199–205. doi:{10.1007/978-3-642-14139-3\\_24}.
- [23] M. Kaczorowski, K.-Q. Xia, Turbulent flow in the bulk of rayleigh-bénard convection: small-scale properties in a cubic cell, *Journal of Fluid Mechanics* 722 (2013) 596–617. doi:10.1017/jfm.2013.74.
- [24] R. Barta, C. Wagner, Large-scale reorientation in cubic Rayleigh-Bénard convection measured with particle tracking velocimetry, *Journal of Turbulence* 26 (2024) 36–49. doi:10.1080/14685248.2024.2436843.
- [25] R. Barta, C. Bauer, S. Herzog, D. Schiepel, C. Wagner, proPTV: A probability-based particle tracking velocimetry framework, *Journal of Computational Physics* 514 (2024) 113212. doi:10.1016/j.jcp.2024.113212.

- [26] A. Savitzky, M. J. E. Golay, Smoothing and differentiation of data by simplified least squares procedures., *Analytical Chemistry* 36 (1964) 1627–1639. doi:10.1021/ac60214a047.
- [27] J. D. Toscano, T. Käufer, Z. Wang, M. Maxey, C. Cierpka, G. E. Karniadakis, Inferring turbulent velocity and temperature fields and their statistics from lagrangian velocity measurements using physics-informed kolmogorov-arnold networks, 2024. doi:10.48550/ARXIV.2407.15727.
- [28] M. Mommert, R. Barta, C. Bauer, M.-C. Volk, C. Wagner, Periodically activated physics-informed neural networks for assimilation tasks for three-dimensional Rayleigh–Bénard convection, *Computers & Fluids* 283 (2024) 106419. doi:10.1016/j.compfluid.2024.106419.
- [29] K. Zhou, S. J. Grauer, Flow reconstruction and particle characterization from inertial lagrangian tracks, 2023. doi:10.48550/ARXIV.2311.09076.